

Laser Writing of Channel Waveguides
into Sol-Gel Alumina Films
—or—
Liquids, Lasers, and Luminescence

A Thesis Submitted 14 May 2007 to the
Department of Physics & Astronomy
of Franklin & Marshall College
in Partial Fulfillment of the Requirements
for the Granting of Departmental Honors

Micah P. Dombrowski
Graduate, May 2007

Copyright © 2007 by Micah P. Dombrowski
Some Rights Reserved

research sponsored by:
The Franklin & Marshall Hackman Summer Research Program
The NASA Delaware Space-Grant Consortium
The Pennsylvania Keystone Innovation Grant Program

The undersigned attest to reading this thesis, and certify that it is—in their opinion—fully adequate in scope and quality for an honors thesis.

(Ken Krebs) Principal Adviser

(Linda Fritz)

(Scott Lacey)

(Christie Larochelle)

(Michael McCooley)

Acknowledgements

I first want to thank everyone in the Franklin & Marshall Physics Department. I've had so many great experiences here that have helped to prepare me for a future in Physics. The personal and exacting nature of the education offered by this department makes it one of the best on campus, and is a boon for all of F&M.

Thanks are surely in order for my honors committee members, Linda Fritz, Scott Lacey, and Christie Larochelle, who had little to no idea what they were signing up to read, and to Michael McCooey, who did know, and still signed on at short notice.

Kudos to Ken Krebs, for giving me this opportunity, for putting up with me for a whole year, and for always being around to interject any required sage advice. I find that after all of this work, I now have amazing confidence in my ability to go on to any lab and make a contribution in Experimental Physics.

Thanks to Steve Spadafore for all his help with the Laser-Writing system. It would not be nearly as awesome without all of his hard work.

Big thanks to Elizabeth Praton, for making me write a paper for my independent-study last year. This thesis would be sorely lacking if I hadn't had that experience.

Props to Mark Lombardi, for all his research on Cr^{3+} spectra in alumina, and especially for letting me swipe his plots.

“Yo,” to all of the other physics newbies. Special thanks to Tim, whose constant insults and discouragement kept me going, just out of sheer spite, to Zach, for providing the comic relief, and to Brian: finally, another Dream Theater devotee.

Thanks to Rick Kipphorn, for giving me a nudge when I really needed it.

My gratitude to Stephan and Kim Williams, for giving me a place to escape to on Thursdays. Now, who knows what kind of trouble I’ll get into?

Also, thanks to members of The Herodotus Society, for being a continuing source of friendship and support.

I must thank my mother for giving me what I needed to make it through these years, for setting a good example through her own academic efforts, and for surrounding me with books since before I could even hold them, all ensuring that I would not only be a nerd and a geek, but proud of it.

Finally, I’d like to thank the Sun, since most everybody else seems to take it for granted. Good, old Sol: without it, we’d never get to wear shorts and sunglasses, and that’s just not cool. Daddy-O.

for Bill

I miss Bill.

Abstract

If a method can be found to heat-treat arbitrary, narrow areas of a sol-gel derived alumina thin film, it will allow the creation of density gradients in the film. In such transparent alumina films, a density gradient would correlate with an increase in the index of refraction, yielding channel waveguides. Channel waveguides in alumina thin films have prospective applications in chemical sensing and optical computing. We developed a system to ‘write’ channels into thin films using an infrared laser, created samples of sol-gel alumina and treated them in our system, and studied the results using near-field optical spectroscopy. We find that thin films of alumina are very sensitive to the sol-gel recipe used, that the process of densifying alumina solids is sensitive to a large number of parameters including laser power and exposure time, and that the laser-imparted heat dissipates extremely swiftly within our samples.

Contents

Acknowledgements	v
Abstract	ix
1 Introduction	1
1.1 Transition Alumina	4
1.2 Sol-Gel Alumina	6
1.3 Laser Heating	6
2 Sol-Gel Alumina	7
2.1 Sol Preparation	8
2.2 Sampling Techniques	9
2.3 Curing	13
3 Laser Heating	17
3.1 The Apparatus	18
3.2 Test Results	19

3.3 Thermal Modeling	26
4 Trivalent Chromium	29
4.1 Cr ³⁺ in Alumina	30
5 Near-Field Optical Spectroscopy	35
5.1 NFOS System	36
5.2 NFOS Results	37
6 Conclusions & Future Directions	43
A Heat-Flow Modeling	47
A.1 Separation of Variables	48
A.2 Fourier's Trick	50
A.3 Numerical Solutions	52
B Optical Notes	55
B.1 Plasma Lines	55
B.2 Focus Width	56
Bibliography	59

List of Figures

1.1	A depiction of a waveguide	2
1.2	A map of transition alumina phases	5
2.1	A flask of alumina sol	10
2.2	A small monolith of alumina	12
2.3	A sample piece of alumina	14
2.4	A drip-coated film	15
3.1	A schematic of the heat-laser writing setup	20
3.2	The completed laser-writing setup	21
3.3	One of the first laser-densified films	23
3.4	A 400×, transmission-lit view	24
3.5	An edge-on, 400×, transmission-lit view	25
4.1	The 3d ³ Tanabe-Sugano diagram	31
4.2	Typical Cr ³⁺ spectra in alumina.	33
5.1	A diagram of a NFOS system	38
5.2	A picture of our NFOS table in action	39
5.3	A position vs. wavelength contour plot	40
5.4	A relative intensity vs. wavelength view	41
5.5	A relative intensity vs. position view	42
A.1	A numerically-derived solution for u	53
B.1	Laser intensity vs. position	57

Chapter 1

Introduction

Optical gradients are precisely what is needed in order to create channel waveguides. In optical waveguides such as fiber-optic cables, materials are combined such that there is a gradient in the index of refraction. This optical gradient yields total internal reflection for some wavelengths, allowing directed, near-lossless transmission of light. A depiction of the internals of a waveguide is shown in Figure 1.1. In a channel waveguide, we confine the structure to a near-two-dimensional realm, creating a surface path through which we can direct light. If a linear, defect-free optical gradient can be produced on a surface, we can guide light across it.

Alumina (aluminum oxide, Al_2O_3) has nice optical and material properties that warrant study. It has several optically clear structural forms, including single-crystal α -alumina (sapphire, corundum, ruby), and the transition alumina phases known as

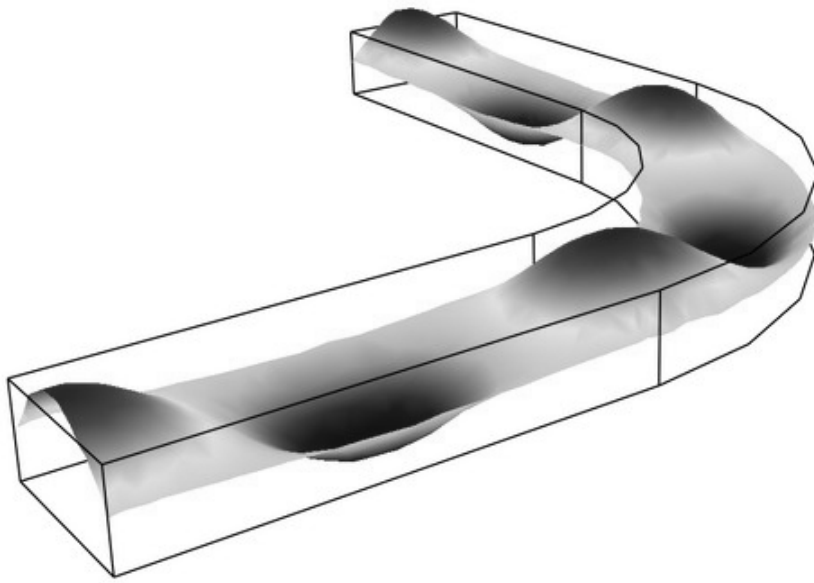


Figure 1.1: A depiction of a waveguide with a curve in it[4].

θ and γ . When α is doped with chromium, it strongly absorbs blue and green, and emits at two well-known wavelengths in the red range—giving the characteristic color of ruby. When θ is similarly doped, it absorbs the same blue and green wavelengths, but emits at slightly different ranges from α , giving a distinct spectra. Crystalline and ceramic forms of alumina have very high thermal conductivity (they feel cold to the touch), and high melting points (approximately 2000°C). Of specific interest—and the main motivation for this study—is that θ alumina made with a sol-gel process has a higher index of refraction than γ alumina, because of its higher nanocrystalline density. This implies that the creation of optical gradients in sol-gel alumina may be made possible through the creation of density gradients.

There are two currently-predictable possible uses for thin-film waveguides in alumina, one of which lies in chemical sensing. The porous nature of sol-gel alumina combined with its catalytic surface states means that it absorbs chemicals from the air¹[1]. If a thin film of alumina with a working waveguide through it is doped such that it only absorbs *specific* chemicals, the absorption of those chemicals in the waveguide-zone will change the way light travels through the waveguide. Thus, by detecting these changes in light, we can tell if a substance is present in the air.

A long-term application is in optical computing. Clearly, any technology for precisely routing light has possible applications in this field; however, it is notable that

¹This is actually a problem in synthesis: alumina samples tend to absorb ambient water vapor.

alumina is possessed of two traits highly desired in computing: high thermal conductivity, and high operating temperature (the waveguides in question would be stable at temperatures up to 750°C).

1.1 Transition Alumina

The sol-gel derived alumina in this study can take several paths towards its most-dense (ceramic/polycrystalline α) form. The phases in between are known as transition aluminas, and the groupings they fall into are outlined in Figure 1.2. The alkoxide, sol-gel-derived alumina we seek to make use of follows the path second from the top in this figure, and climbs towards α as the density of the alumina is increased. After leaving the amorphous boehmite stage, there exist four distinct phases, traditionally referred to as γ , δ , θ , and α alumina. In standard sol-gel alumina (uniformly densified in an oven), these phases are sharply defined by their lattice structures, i.e., they change lattice configurations quickly once the alumina reaches a density such that a new ordering is more energetically favorable[10].

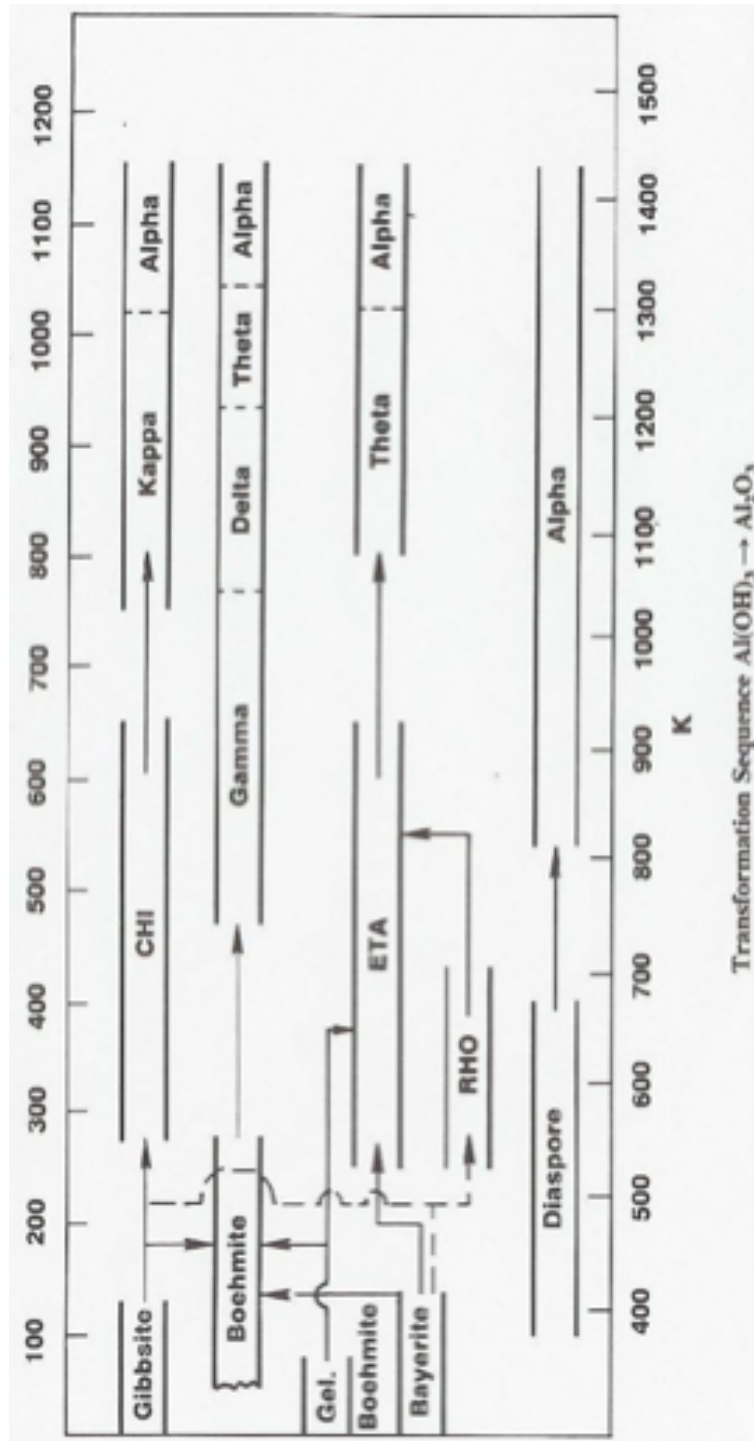


Figure 1.2: A map of transition alumina phases[15]. The path that our sol-gel alumina takes is second from the top.

1.2 Sol-Gel Alumina

The θ sol-gel alumina which we are interested in—attained at temperatures between 900°C and 1050°C^2 —is the non-ceramic stage at which nanocrystalline alumina becomes most optically transparent. Moreover, the index of refraction of the material is larger in θ than in its precursor, γ , because of structural changes and the elimination of volatile remnants from the sol-gel. What this implies is that interesting and useful optical gradients can be created, if a method can be found for heating and densifying only specific regions of a piece of alumina.

1.3 Laser Heating

Within the past few decades, a method for reliably and repeatably heating small regions of a material has become widely available: heat lasers. A good infrared laser with a Gaussian power distribution is reliable, yields consistent results, and can be focused and manipulated into a wide variety of configurations.

It is therefore possible that a focused heat laser beam can be used to ‘write’ dense channels into sol-gel alumina, thus creating channel waveguides in thin films of sol-gel alumina.

²It is notable that the temperatures at which these transitions occur are modified by lanthanide impurities[11], which could prove useful in an application.

Chapter 2

Sol-Gel Alumina

The sol-gel process is a wet chemical process for creating solids[7]. Appropriate chemicals for the desired material are combined, and allowed to react, creating a solution of nanocrystals of the material suspended in fluid (generally a water-alcohol mixture). This fluid is then air-dried or boiled to a thick fluid or gel state, poured, dripped, spun, or otherwise manipulated into a desired shape, and cured through heating. Heat removes the volatiles in the gel, leaving a progressively denser matrix of nanocrystals, until—at some maximum heat—the material reaches its most-dense form, a ceramic.

By itself, the sol-gel process is useful in many materials for several reasons. The cleaner the synthesis environment, and the purer the ingredients, the more pure the end product is. This can potentially yield much better results than direct mineral-to-solid synthesis. The maximum temperature required to make a fully densified chunk

of the material is much less than that required to mold a similar chunk by melting and casting¹, and the sol-gel process requires much less (generally zero) handling of the hot substance.

2.1 Sol Preparation

Samples for this study were grown in-house, at the Franklin & Marshall College Physics department, using an alkoxide-based method developed by B. E. Yoldas[16, 17]. Our only modification to Yoldas' recipe is the addition of dopants—specifically, chromium (to give our final products ruby-like optical properties) and europium (chosen for its well-studied optical properties in alumina)—in the form of salts.

We start by adding aluminum-isopropoxide and the dopants to a small amount of isopropyl alcohol, and mixing thoroughly. The solution is then hydrated by the addition of enough distilled water to yield a 100:1 water:alkoxide molar ratio. This ratio ensures that there is enough water to go around, and as a bonus gives enough mass to absorb the heat released in the exothermic alkoxide-water reaction. The mixture is heated and stirred for about a half-hour, and then raised to at least 80°C before the addition of acid. We chose to use nitric acid to peptize our sol—enough of it to yield a 0.07:1 acid:hydroxide molar ratio, which ensures gelling at a low volume, and thus yields a gel with a high alumina nanocrystal concentration[16]. This final

¹An example: the melting temperature of silica glass is (depending on composition) 1400-1600°C. The temperature required to fully densify a chunk of sol-gel silica is approximately 1000°C.

solution is kept above 80°C, and stirred for at least 30 minutes (longer is better). Finally, the sol is removed from heat, and left to age for hours to days to months. To a point, aging yields a more thoroughly reacted solution, with a higher viscosity—in the parlance of wine, it gives the fluid ‘legs.’

In the course of this study, several batches of this Yoldas brew were made. The clearest sols (see Figure 2.1), and sturdiest final products were achieved when using a ‘reflux’ apparatus during the liquid mixing and boiling stages. Reflux systems allow lossless boiling by running the vapor through a water-cooled tube, condensing it and returning it to the main body of fluid. By enabling a full boil to be maintained for hours, or even days, refluxing ensures that maximal reactions take place at each stage of the process.

2.2 Sampling Techniques

A sol can be manipulated for sampling by many methods. We made use of three: spin coating, evaporative coating, and monolith casting. Some care must be used in handling these samples, as they are still very porous and contain organics, and are therefore rather fragile.

- Spin coating yields extremely thin films. Substrate discs (we used both glass and sapphire discs) are vacuum-adhered to a high-speed motor, and can be spun at rates from 100 rpm to 6000 rpm. The sol is dripped onto the substrate

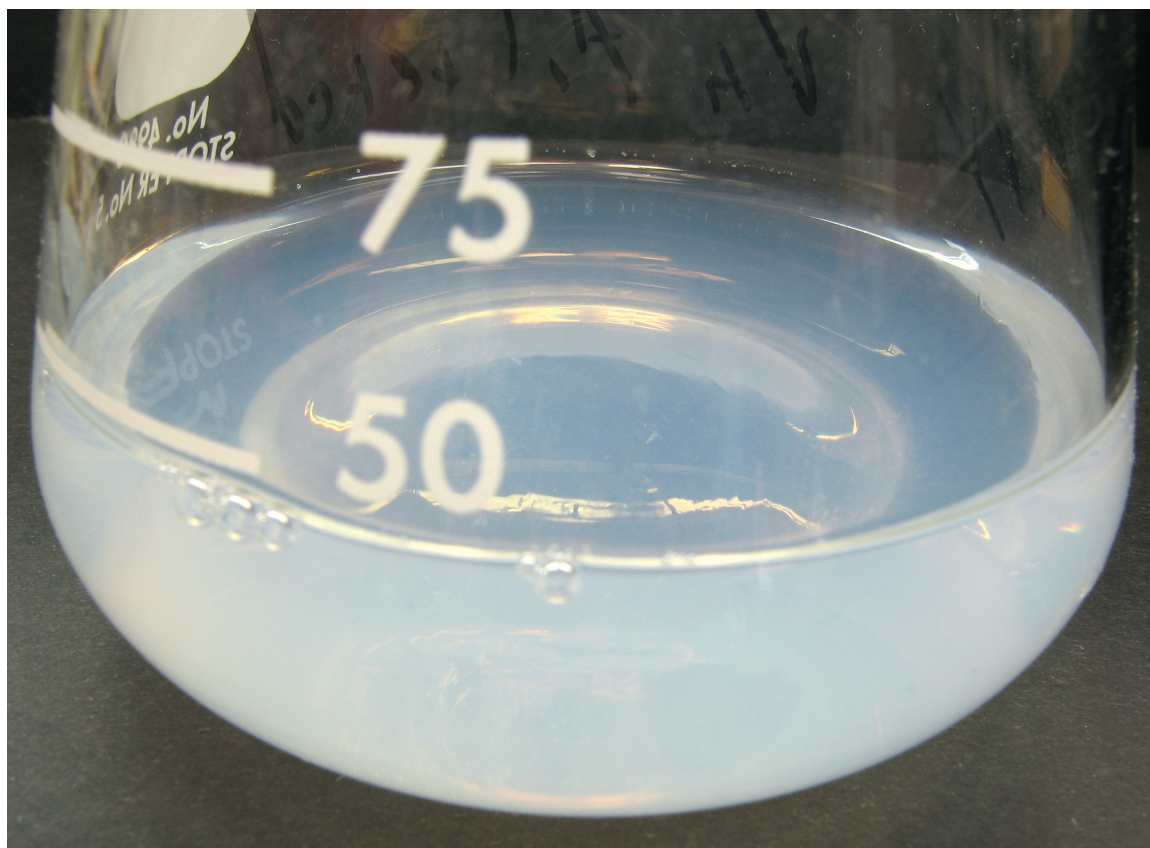


Figure 2.1: A flask of high-quality alumina sol. This batch was refluxed for several days, and at the time of this picture had aged for over three months.

either before spin-up, or during the spin, and the spinning immediately casts off most of the fluid, leaving behind a very thin coating, which air-dries almost instantly. A benefit of this method is that only a few milliliters of fluid are needed per sample. A downside is that small substrate size, surface tension, and the spinning can conspire to make the resultant films anisotropic.

- Evaporative coating is a way of making thicker films. In this method, either the sol is dripped on in any amount that will stick to the substrate because of surface tension, or a slide or substrate can be dipped into a pool of the sol. The sample is then left to air dry, which can take several hours. This method uses more fluid, but is still quite thrifty; however, on small substrates, isotropy is still elusive.
- Large amounts of the sol can be used to make solid ‘monoliths’ of alumina. Generally, the fluid is first boiled to a high concentration (nearly to the gel state) before being poured into molds. Any size mold can be used, but even very small monoliths can take days to dry.

A typical alumina solid is shown in Figure 2.2.



Figure 2.2: A small, sample monolith of alumina. Note the blue sheen, which is characteristic of Yoldas alumina sol-gels.

2.3 Curing

After thoroughly air drying, the sample must be cured in a furnace—in this study, all samples were taken to 750°C. This removes the remaining volatiles, shrinking the sample to about 40% of its initial volume, and brings the alumina firmly into the γ phase. All samples can be put through a long curing program, which slowly heats in stages, allowing plenty of time for volatiles to make their way out of the alumina; however, with thin films it is also possible to ‘flash’ cure (push into a hot furnace, and pull out in a few minutes), since the relatively large surface-area to volume ratio means that volatiles can escape almost instantaneously. After curing, the samples (such as that in Figure 2.3) are quite robust, as they are pure—though porous—alumina.

In our experience, thin, spin-coated films and monoliths both handle air-drying and curing quite well. Curing bonds spin-coated films to their substrate—especially sapphire substrates—and generally reduces the size of monoliths, while maintaining their integrity. Evaporatively-coated films are another story: even during the air-drying stage many such films will start to show cracks, and, as in Figure 2.4, during curing the vast majority of these films crack and peel from their substrates. This occurs because of lateral stresses imposed as the sample shrinks while bonded to its substrate.



Figure 2.3: A typical, fully-cured sample of alumina made through the Yoldas sol-gel process. The yellow tint is a sign of the chromium doping.



Figure 2.4: A drip-coated film: thick, but unstable.

Chapter 3

Laser Heating of Alumina

We determined that a 10.6 μm laser was a suitable choice for our attempts to write waveguides. Light at this wavelength is very quickly and thoroughly absorbed by a vast majority of materials, with a very shallow penetration depth. Similar lasers have been used for in-depth studies of sol-gel silica, and the depth of penetration has been calculated to be approximately 10 μm [5]. This implies that only slightly more than 10 μm depth of film is needed for acceptable channel creation. Over the course of this study, we designed and built a laser-writing apparatus, performed some preliminary tests on thin spin-coated films and monoliths, and began to mathematically model our results.

3.1 The Laser-Writing Apparatus

We designed and constructed a computer-controlled laser writing apparatus using a 30 W, 10.6 μm , CO₂ laser¹. As this wavelength of light is invisible to the naked eye, and is so readily absorbed by matter, a number of special considerations had to be made in directing and controlling the beam.

Polished copper is an excellent reflector of 10.6 μm light, and a moiety of copper provides a large heat sink for any of the beam that is absorbed; however, copper tarnishes very quickly. To prevent oxidation, we electroplated a thin coat of gold onto our copper mirrors.

A way of aiming the laser at its target pre-firing was required, so we made use of a zinc-selenide window as a beam collineator. Zinc-selenide has a grain size of about 70 μm , and so transmits a wide range of infrared radiation, including 10.6 μm . It appears translucent-yellow to the eye, and reflects approximately 50% of a visible-light laser. We used this window to bring the light from a simple red-diode laser pointer collinear with the CO₂ laser beam, allowing us to aim the heat laser using the pointer's red dot.

The CO₂ laser outputs an approximately 3mm-wide beam, so a high-quality, gold-coated, 10cm-focal-length, 90°-deflection, parabolic mirror was used to focus the beam on the target. This also increased our maximum possible heating ability: with this

¹30 W maximum power. In our tests we never went above 10% power without destroying samples.

focus, all of the laser's power output can be directed at an extremely small area.

In order to write channels along a sample, either the sample or the laser beam needs to move. As moving the beam from a Class IV heat laser is generally a bad idea, we made use of two computer-controlled 1-inch translation stages as sample mounts. Short-range stages such as these allow highly-repeatable sub-micron movement control.

In the final setup, diagrammed in Figure 3.1 and seen in Figure 3.2, the laser is given a 1-meter dispersion path—this is needed to allow a more-precise end focus, as a larger beam going into the parabolic mirror yields a finer focus on the other side. Two copper mirrors were required to allow full control of where the beam strikes the parabolic mirror, and at what angle it does so. Finally, safety regulations state that Class IV laser beams must be fully enclosed during operation, so a plexiglass-walled cage was built to house the laser. While plexiglass cannot withstand even the unfocused beam for more than a couple of seconds, it does glow and emit fumes when hit, hopefully giving the user sufficient warning of a catastrophic failure.

3.2 Preliminary Test Results

We conducted preliminary tests using this setup. Our aim was to find—by iterative adjustment—the correct parameters to make a good channel waveguide. We examined our results under 20x and 400x magnification.

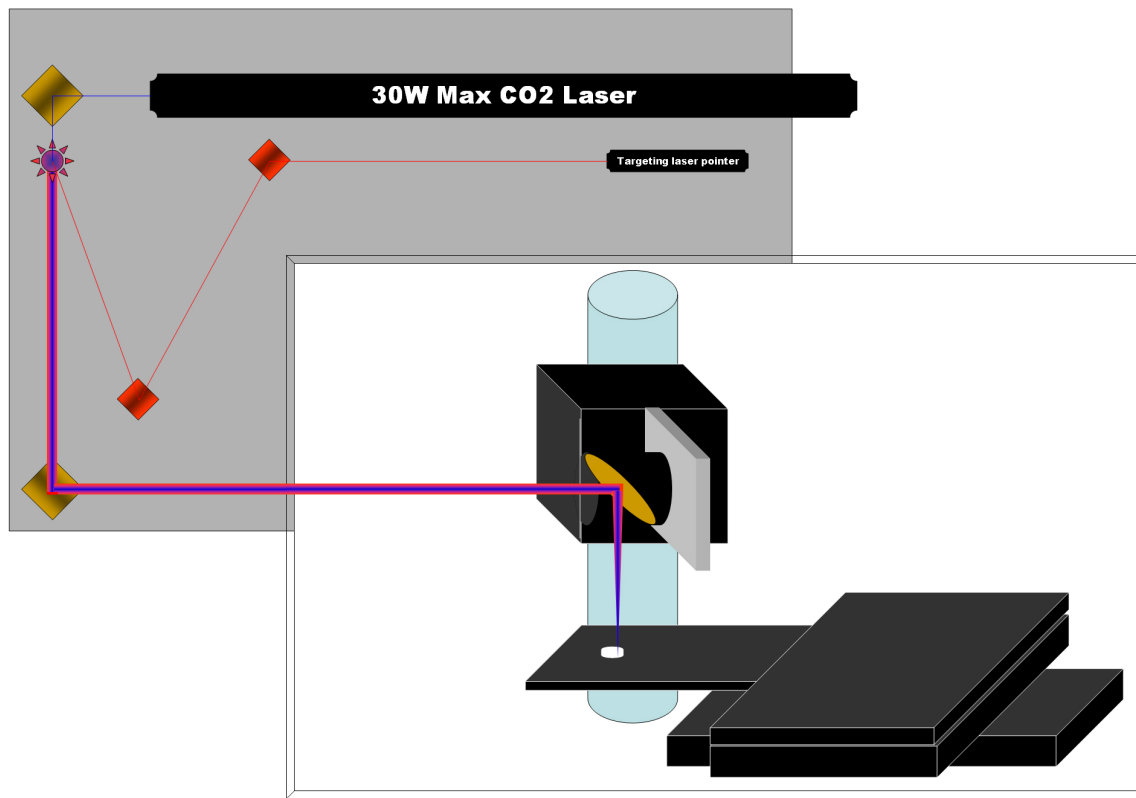


Figure 3.1: A schematic of the heat-laser writing setup, showing the copper mirrors, pointing-beam collimation, focus, and target area.

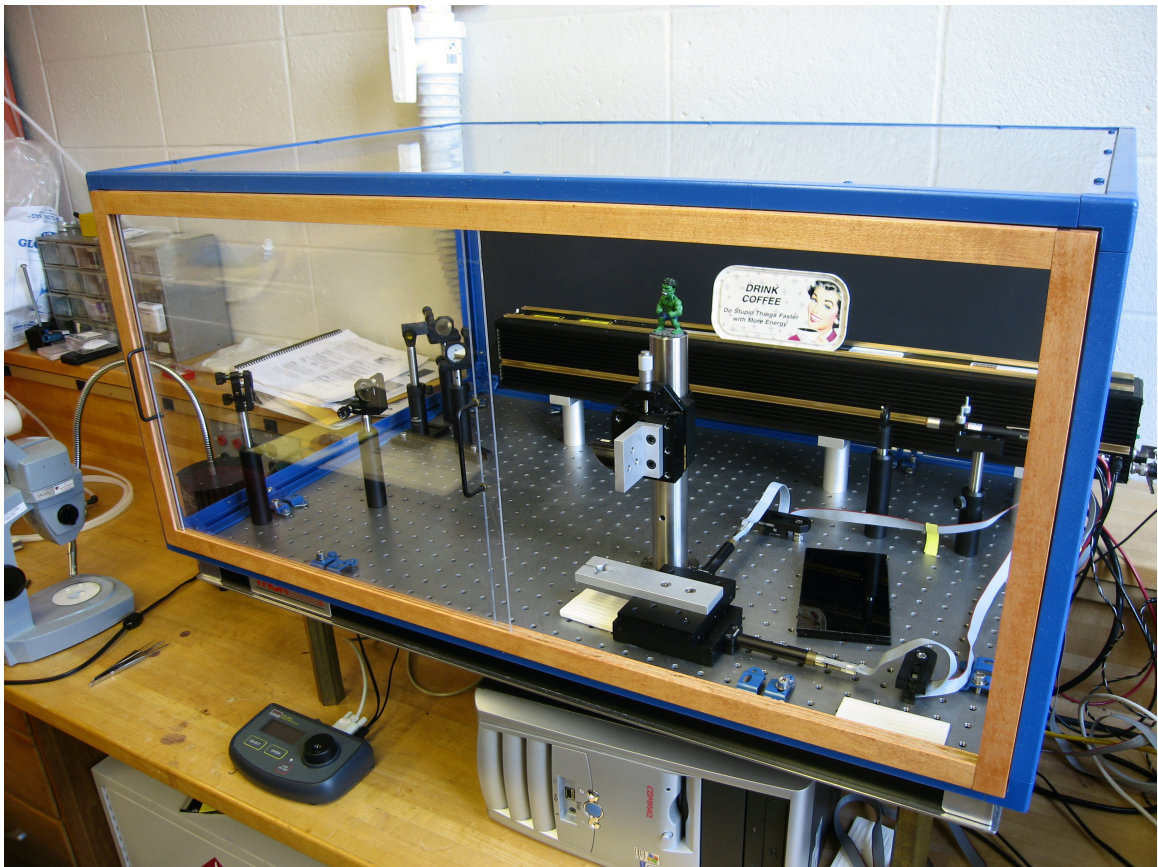


Figure 3.2: The completed laser-writing setup. The blue-railed, Plexiglass enclosure provides air-flow control, and complies with safety codes regarding Class 4 lasers. Plus it looks really sweet.

Spin-coated films show evidence of laser densification, as seen in Figure 3.3, where the film is on a glass substrate; however, most of the heat is transferred laser \rightarrow substrate \rightarrow film. We know this because of the lack of effect on films laid on thermally-conductive sapphire substrates, and because of evidence of laser-melted glass on the edges, as in Figure 3.5. What this implies is that our films are *too thin* (less than $10\ \mu\text{m}$), and most of the laser is passing right through them. Attempts to couple laser light into these channels have been unsuccessful, most likely because of the extreme thinness of the films. While the lased region is seen to be smoother and denser than the surrounds in Figure 3.4, when viewed edge-on in Figure 3.5, we see that the film is so thin that its breadth cannot be seen under $400\times$ magnification. This implies that these films are less than $1\ \mu\text{m}$ thick—too thin for visible light to effectively couple in.

In studies of laser heating of silica, it was found that the parameter space for laser creation of density gradients has both time and power dimensions, and that the ranges for quality results are quite narrow. It would appear that we have found that this holds for laser heating of alumina. Also, in these early tests, we expanded the parameter space to untenable dimensionality, with the addition of film thickness, film anisotropy, substrate reactivity, and simply by the fact that our target was moving. To cut the parameter space back as far as possible, we decided to follow the same paradigm used in silica studies[2, 3, 5]: modeling the thermal properties of an alumina monolith

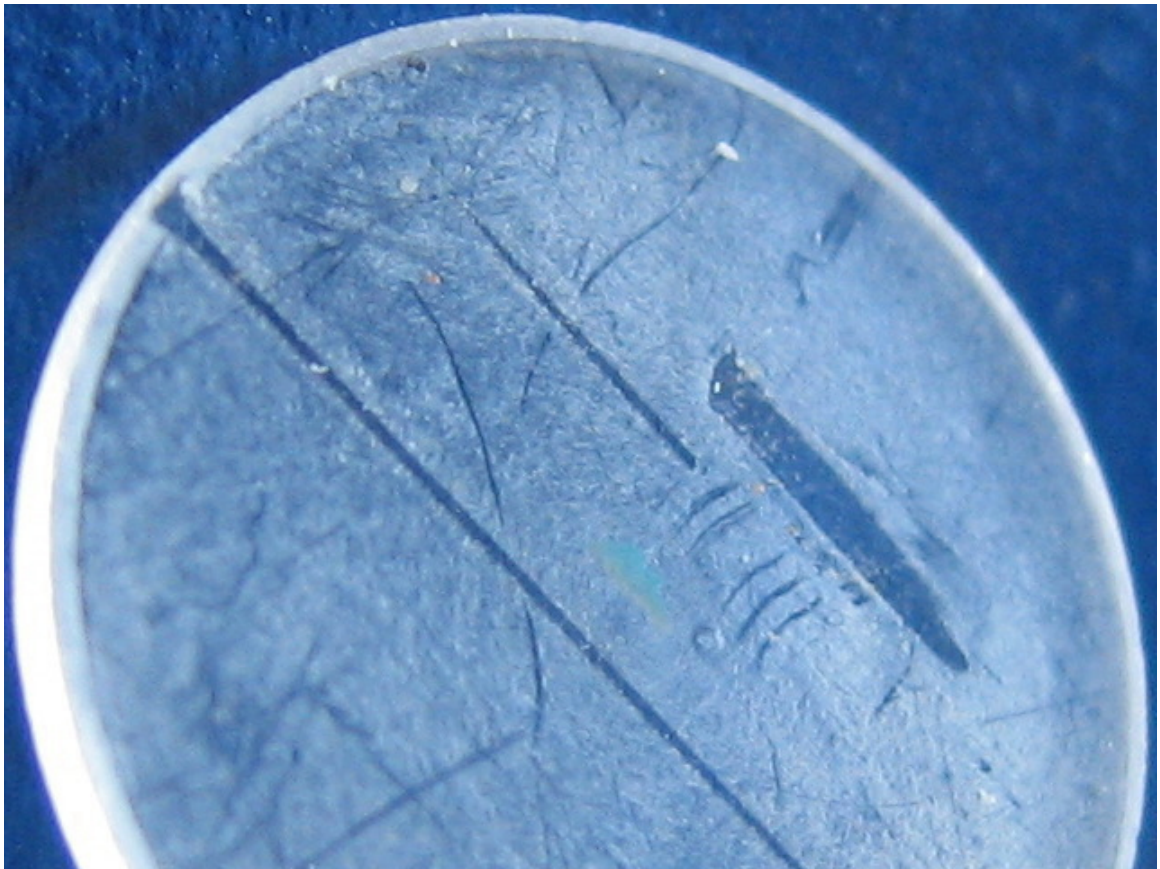


Figure 3.3: One of the first laser-densified films to come out of our procedure.

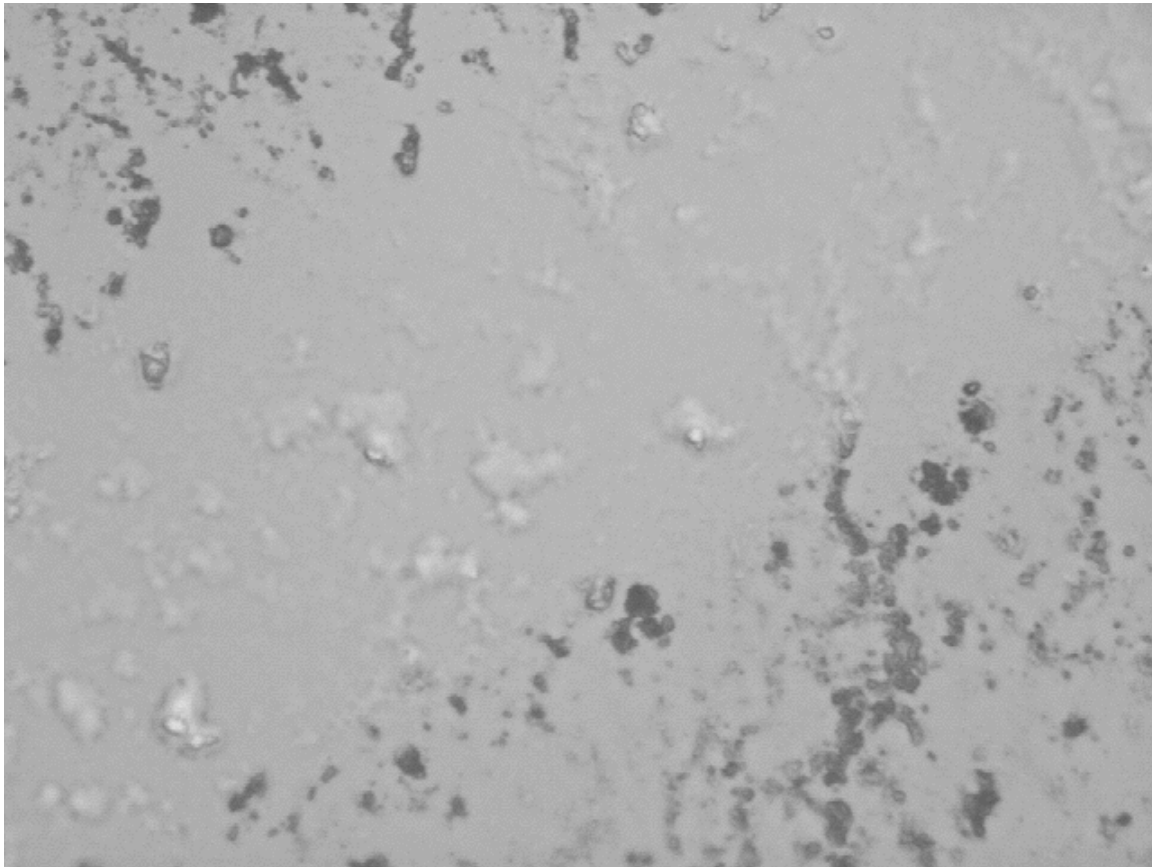


Figure 3.4: A 400 \times , transmission-lit view of a thin film with a laser-densified channel on it. Note that there are many fewer 'craters' on the surface in the densified region.



Figure 3.5: An edge-on, 400 \times , transmission-lit view of the film in Figure 3.4. The film is so thin, its breadth cannot be seen at this magnification. At the edge of the laser-densified region, some melting of the glass substrate can be seen.

when laser-heated at a point (creating not a channel waveguide, but a microlens), and performing some basic tests towards aligning our model to the real world.

3.3 Thermal Modeling of Laser-Heated Alumina

Modeling the heat flow from a stationary, point- or Gaussian-source laser is an attractive option for determining the correct parameter-space coordinates for making good-quality waveguides; however, this problem turns out to be non-trivial. In most models of laser heating, it is assumed that a “quasi-steady state” is reached, i.e. that the laser is at a high enough power and lingers on a region of the target long enough that an equilibrium state is reached[8, 9, 12]. In such a state, there is no change in time if the coordinate system is taken to be moving with the laser strike point (thus “quasi-steady state”). In the sol-gel silica laser heating studies, one dimension of parameter space is the amount of time the laser is left on, which implies that a quasi-steady-state configuration is not assumed[3]. In practice, this means that a thermal model will be time-dependant, and so the full time-dependant heat flow differential equation,

$$\frac{1}{\alpha^2} \frac{\partial u}{\partial t} = \nabla^2 u \text{ (where temperature } u = u(r, \theta, t)), \quad (3.1)$$

must be solved.

While it is not clear that our samples are perfectly homogeneous², we assume

²In fact, there are hints otherwise: during laser heating samples have been seen to randomly flare

homogeneity for a first approximation. With this assumption, a model can use a spherical coordinate system, and discard the azimuthal angle, taking heat dissipation to be azimuthally uniform.

It is also quite clear that the physical properties—thermal conductivity, specific heat, and density—that express themselves in the α constant in Equation 3.1 will not in reality be fixed. The very process we’re trying to model causes the alumina to become more dense, and with this density change comes increased phonon transfer and large structural changes. Now, without these changes we would not have the index of refraction changes we want to use, nor the chromium spectral changes we will make use of later to study these solids, but the fact that there is implicit dependence of α upon u itself blows the complexity of this problem up immensely. Nevertheless, we believe it is possible to get a basic picture of the flow of heat through these samples while taking α to be constant. It is, in fact, a good thing that we believe so, because it would appear that there have been no significant studies of the thermal properties of transition alumina, and so the only data we have for α must be based on the properties of α alumina.

While we have, thus far, been unsuccessful in finding an exact solution for Equation 3.1 in our approximation, we have made significant progress, and our work is recorded in §A.

as they become denser, and to crack in non-symmetric shapes.

Chapter 4

Trivalent Chromium Spectra

The Cr^{3+} impurity ion energy levels are strongly affected by the strength and symmetry of the crystal field in which the ion is embedded. In transition alumina, a chromium impurity absorbs strongly at 543nm (green), but the crystal field modifies where it subsequently emits. The $3d^3$ electron level in Cr^{3+} probes crystal field strength effectively because of unpaired electrons in the d-orbital, which are strongly affected by nearby atoms in the lattice¹[6]. This energy-level sensitivity is visualized in plots of the energy levels (for perfect octahedral symmetry) vs. crystal field strength about the ion known as Tanabe-Sugano diagrams[14]. A use for this probe lies in the fact that the crystal field strength and configuration changes in our alumina samples as density is increased[13].

¹In the case of alumina this is a 'box' of six oxygen atoms.

4.1 Cr^{3+} Spectroscopy in Transition Alumina

The relevant Tanabe-Sugano diagram for trivalent alumina ($3d^3$) is seen in Figure 4.1, as are approximations of the energy levels currently believed to correspond to θ and α alumina. This diagram is quite accurate for α —as is the α line we draw on it—because the crystal structure in α is very close to having perfect octahedral symmetry. The dominant emission from α has its origin in broad green absorption in the 4T_2 level, and emission from the 2E doublet, yielding two close, sharp lines (known as the ‘ruby R-lines’ for historical reasons). The θ line, on the other hand, is very much an approximation.

Logically, as θ is less dense than α it should have weaker crystal fields surrounding its chromium ions, and we should see features in α spectra shifted to longer wavelengths in θ ; however, we actually see shorter-wavelength features. This implies that there are other structural differences between θ and α and that the transition in phases causes a pronounced change in the symmetry of ion sites. This means that new energy-level diagrams must be calculated to reflect this non-octahedral symmetry. Recent work in our lab suggests that θ alumina has its 2E doublet shifted to higher energies relative to its position in α [11].

Though we do not yet know the exact structure of θ , its emission is invariably distinct from α , and both are distinct from γ , which has no sharp features. Typical spectra for pure (furnace-cured to a given stage) γ , θ , and α are shown in Figure 4.2.

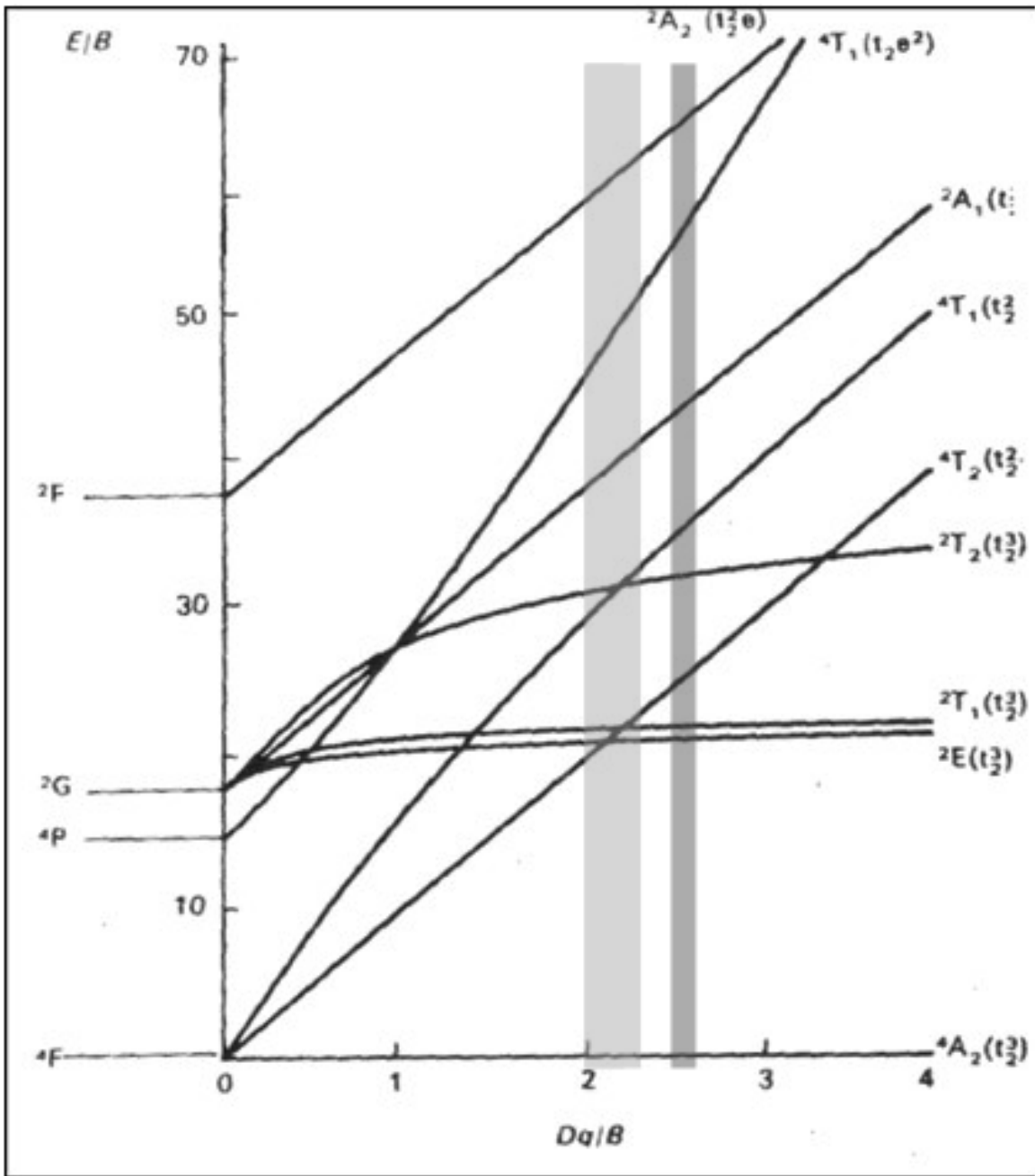


Figure 4.1: The $3d^3$ Tanabe-Sugano diagram, which is appropriate for trivalent chromium. The approximate regions of the diagram which correspond to θ (light) and α (dark) alumina are marked. Note that, because of structural differences, this diagram is very accurate for α , but only approximate for θ .

We can use these differences to distinguish between phases in a sample; moreover, in mixed-phase samples, we can use the ratio of intensities of the different signals in a single spectra to determine how efficiently we are converting the alumina.

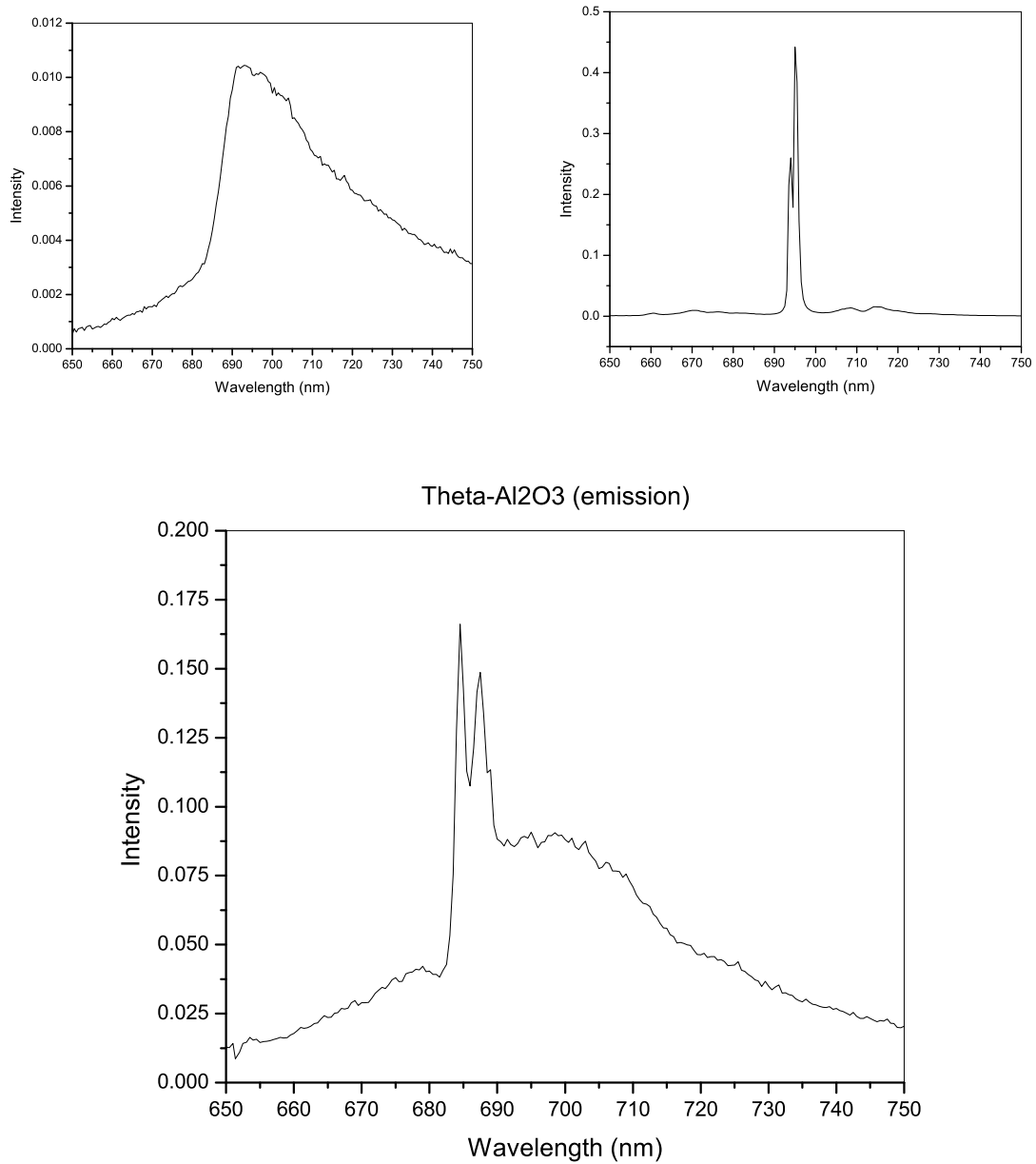


Figure 4.2: Typical spectra (relative intensity vs. wavelength [nm]) for trivalent chromium in γ (top left), α (top right), and θ alumina. Note that in α , the two emission lines are referred to as the ‘ruby R-lines’ for historical reasons.

Chapter 5

Near-Field Optical Spectroscopy on Laser-Heated Alumina

We need a method of studying how the heat laser is densifying and causing transitions on small regions of our sample, and we find such a method in a spectroscopy technique we refer to as Near-Field Optical Spectroscopy (NFOS). The ‘near-field’ is the range of distances at which the object being studied does not appear point-like, and so we can make local—as opposed to global—observations. In the study of electric and magnetic fields, it refers to measurements made in proximity such that the antenna’s emissions are localizable to specific regions of the antenna. Likewise, while in standard spectroscopy, an entire sample’s emissions are examined, in NFOS, we use precise focusing to localize the region of the sample we excite, and where we look for emissions.

For our purposes, we bring the excitation laser beam in through a microscope objective onto a small area of the sample, and then focus the image seen through the objective onto a monochromator slit. By taking numerous spectra while using a micrometer screw to translate the sample across the objective's field of view, we can get a very precise picture of how regions of our sample are densifying. As both types of coated-substrate sample have—thus far—proven themselves unsuitable, we applied this technique to laser-heated monolithic samples.

5.1 A Near-Field Optical Spectroscopy System

Our basic NFOS paradigm is diagrammed in Figure 5.1. After traversing a long dispersion path (see §B.1), the excitation laser beam (543.5nm HeNe) is brought in perpendicular to the main optical path, and is deflected into the main NFOS path by a prism. It travels through the intermediate optics, and then the microscope objective focuses it onto an approximately 10 μm (see §B.2) spot on the sample. Light returns through the objective, and this collimated output is expanded by a Galilean beam expander. This is necessary so that the deflection prism will not block a significant amount of the emission. The reflected laser light is then filtered out, and the emission is focused into a monochromator slit. By making the sample mount a 2-D micrometer-translatable mount, the objective can be precisely focused on any area of the sample, and translated across segments of it. Our actual setup is seen in 'action' in Figure 5.2.

5.2 Near-Field Optical Spectroscopy Results

We found that the heat from the laser must dissipate extremely swiftly. This can be seen in Figure 5.3: the ruby R-lines characteristic of α -alumina are prominent, and there are no signs of either the lines or the ‘hump’ characteristic of θ . This implies that if there is θ , it is in such small quantities that it is not emitting above the noise level. The relative intensity and shapes of the R-lines are more readily visible in Figure 5.4.

We can see that the densified region is about 400 μm wide in Figure 5.5 of intensity vs. sample position, and it is also notable that there may be signs of the Gaussianity of the CO₂ laser beam showing up in this data. If this is a true showing (i.e. if our intensities are actually absolute), this Gaussian densification would add to the implication that the heat imparted by the laser is dissipating near-instantaneously, and does not heat even immediate neighbor areas enough to create θ .

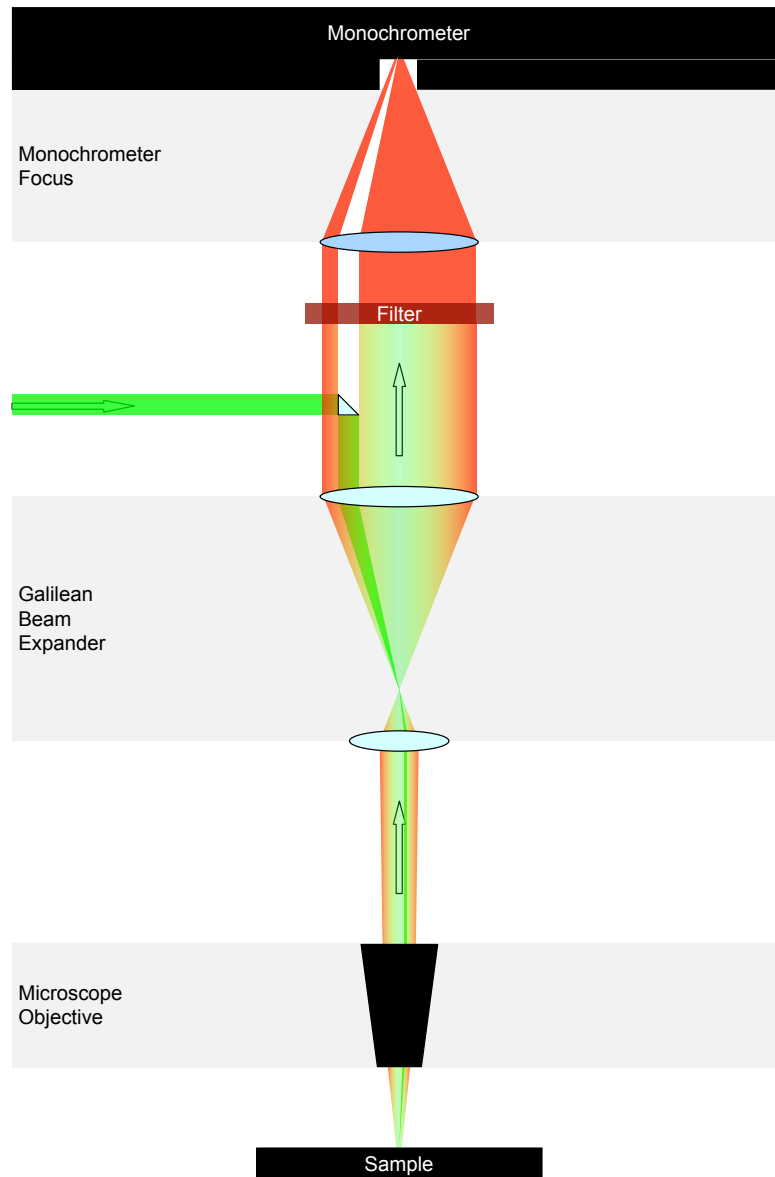


Figure 5.1: A diagram of a Near-Field Optical Spectroscopy system.

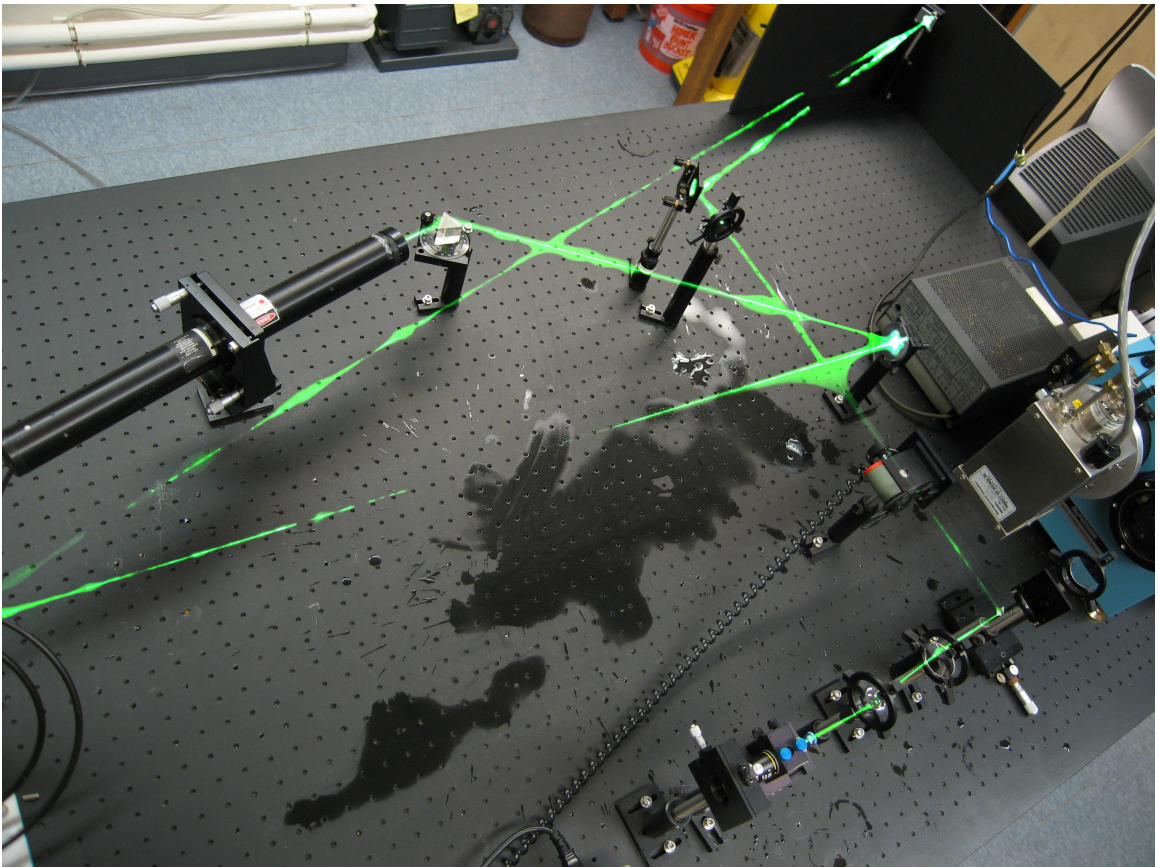


Figure 5.2: A composite picture of our NFOS table. This is a composite of several pictures, some taken with the lights off and excitation laser on (fog provided by dry ice), and some with the lights on. Note the spilled water on the table. Oops.

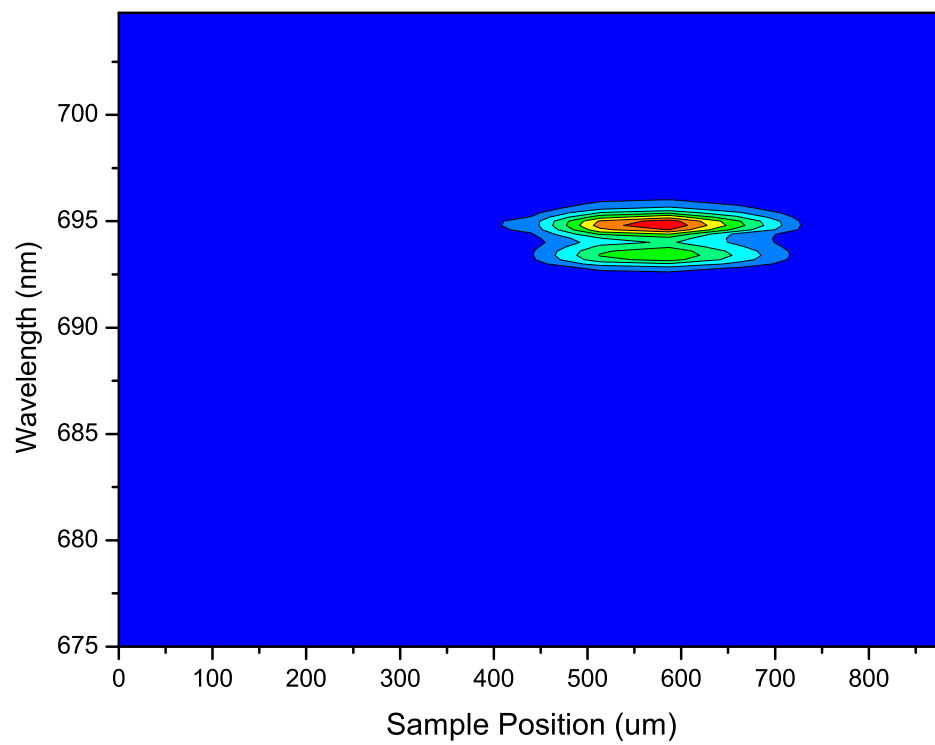


Figure 5.3: A position vs. wavelength contour plot of the NFOS data collected from a typical sample. The ruby R-line positions in both real space and wavelength space are visible.

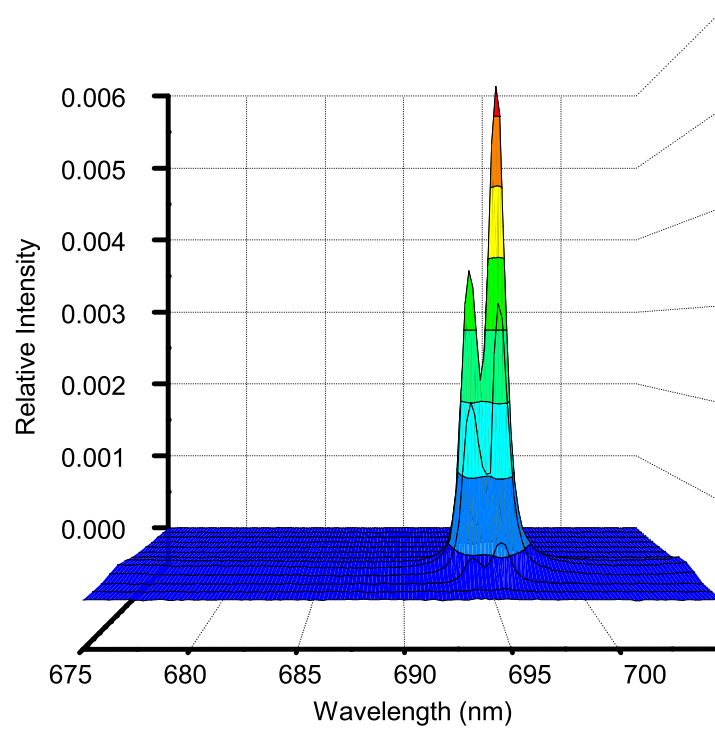


Figure 5.4: A relative intensity vs. wavelength view of the NFOS data collected from a typical sample. From this view, the ruby R-lines the α is emitting are very clear, and it is also clear that there is no significant θ presence in the sample.

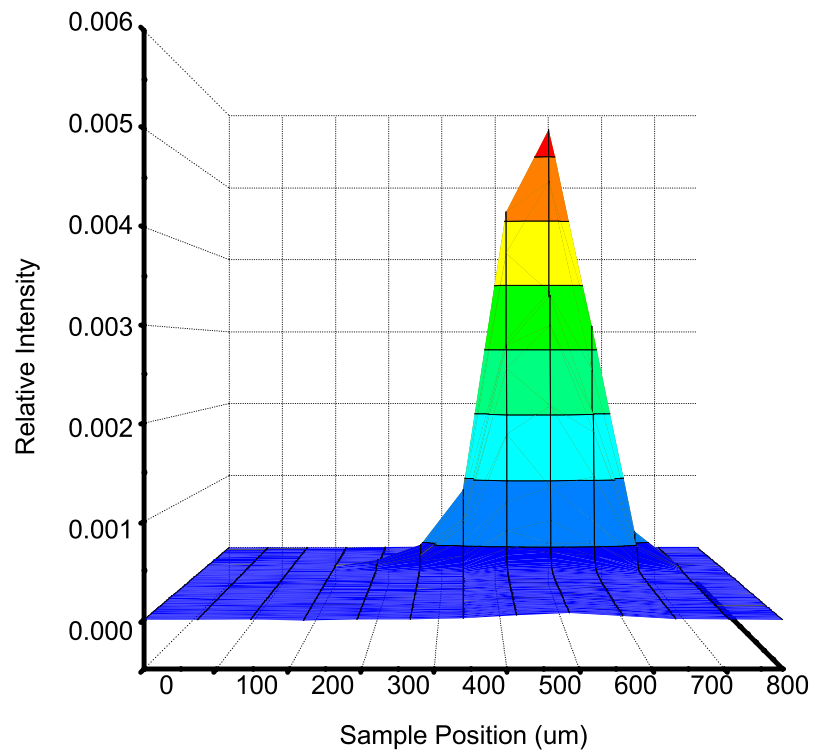


Figure 5.5: A relative intensity vs. position view of the NFOs data collected from a typical sample. From this view it is clear that the region of densification to α alumina is quite sharply defined, and that the densified region is approximately 400 μm wide. Note that there may be hints of the Gaussian power distribution of the CO_2 laser.

Chapter 6

Conclusions & Future Directions

We have designed and built a system to laser-densify sol-gel alumina, applied it to a number of samples, and studied the results using a novel method of optical spectroscopy—all towards a goal of creating channel waveguides in thin films of alumina. To date, we are able to come to a number of conclusions.

Further refinement of alumina sample synthesis techniques is required. Our spin-coated thin films are too thin to absorb a significant amount of the CO₂ laser's power, and our thicker films do not survive curing intact. It may be that our current recipes are fine, and all that is needed is to find the 'happy medium' of film thickness (probably 10-20 μm); however, it may also turn out that our sol-gel recipes need to be modified to yield more resilient pre-cure films. One avenue for such modifications has been studied by Yoldas: different amounts of polymerizing acid yield different

gel volumes, and thus different nanocrystalline densities[16]. Thus by modifying the amount of acid we add to the sol, we may be able to make more- or less-flexible films.

Despite the fact that coating thickness is a confounding factor, we do have evidence that the CO₂ laser can densify small areas of sol-gel alumina. As in prior studies in sol-gel silica, this effect has been found to be very sensitive to laser power and exposure time. Our preliminary tests show that the densification of a region can cause severe stress within alumina solids, leading to fractures. That this does not occur in our thin-film samples implies that this is caused by three-dimensional stresses; however, even in monolithic samples a good mathematical model of heat flow may allow us to determine laser parameters which will densify without ruining samples.

Finally, our NFOS data shows that laser heat is dispersed with extreme swiftness in alumina. More than that, a simple visual inspection of any of the samples prepared for NFOS yields a similar impression. Generally a single white speck appears at the site of the laser heating, and the sample appears unchanged around the speck.

In relation to the end goal of making channel waveguides, these findings generate two notes of interest. It may, in fact, prove impossible to use this type of alumina in this way. If the gradients created around a laser-heated point are too steep, they may turn out to be too insignificant to yield total internal reflection. This does not rule out the possibility of any sort of alumina being used, as the modification of transition temperatures by dopants may make it possible to soften the gradient.

If it turns out that the gradients created by this process are, in fact, usable, the swift heat dissipation will make for very accurate processing. The gradients around the microlenses we have made are about $400\ \mu\text{m}$ wide, but further refinement of the CO_2 beam focus can only improve this. Even with our current, prototype laser-writing optics, we have a theoretical diffraction limit on our focus as small as $25\ \mu\text{m}$; therefore, with careful adjustment, complex channel structures could be written into a very small area.

Appendix A

Heat-Flow Modeling

We seek a function for temperature

$$u = u(r, \theta, t),$$

with r the radial distance, θ the altitudinal angle, and t time.

In order to determine the appropriate u for our model, we must solve the heat-flow differential equation,

$$\frac{1}{\alpha^2} \frac{\partial u}{\partial t} = \nabla^2 u \quad (\text{where } u = u(r, \theta, t)). \quad (\text{A.1})$$

A.1 Separation of Variables

We attack Equation A.1 using separation of variables, i.e. assuming that $u = S(r, \theta)T(t)$. Expanding A.1 with this assumption, we have

$$S \frac{dT}{dt} = \alpha^2 T \nabla^2 S,$$

and dividing by u yields

$$\frac{1}{T} \frac{dT}{dt} = \alpha^2 \frac{1}{S} \nabla^2 S = -\tau^2, \quad (\text{A.2})$$

where we set both sides equal to the constant $-\tau^2$, for the usual reasons. With $\frac{dT}{dt} = -\tau^2 T$, it is clear that

$$T(t) = Ae^{-t\tau}. \quad (\text{A.3})$$

Expanding the spacial side of Equation A.2 and assuming $S(r, \theta) = R(r)\Theta(\theta)$, we find that

$$\begin{aligned} \frac{1}{r^2} \frac{\partial}{\partial r} \left(r^2 \frac{\partial}{\partial r} R\Theta \right) + \frac{1}{r^2 \sin \theta} \frac{\partial}{\partial \theta} \left(\sin \theta \frac{\partial}{\partial \theta} R\Theta \right) &= -R\Theta \frac{\tau^2}{\alpha^2} \\ \Rightarrow \frac{1}{R} \frac{d}{dr} \left(r^2 \frac{d}{dr} R \right) + \frac{1}{\Theta \sin \theta} \frac{d}{d\theta} \left(\sin \theta \frac{d}{d\theta} \Theta \right) &= -\frac{\tau^2}{\alpha^2} r^2 \\ \Rightarrow \frac{1}{R} \frac{d}{dr} \left(r^2 \frac{d}{dr} R \right) + \frac{\tau^2}{\alpha^2} r^2 &= -\frac{1}{\Theta \sin \theta} \frac{d}{d\theta} \left(\sin \theta \frac{d}{d\theta} \Theta \right) = n(n+1). \end{aligned} \quad (\text{A.4})$$

Considering the Θ part of Equation A.4, it is easy to see that

$$\begin{aligned}
\frac{d}{d\theta} \left(\sin \theta \frac{d}{d\theta} \Theta \right) &= -n(n+1)\Theta \sin \theta \\
\Rightarrow \cos \theta \frac{d\Theta}{d\theta} + \sin \theta \frac{d^2\Theta}{d\theta^2} &= -n(n+1)\Theta \sin \theta \\
\Rightarrow \cos \theta \frac{d\Theta}{d\theta} + \sin \theta \frac{d^2\Theta}{d\theta^2} &= -n(n+1)\Theta \sin \theta \\
\Rightarrow \Theta'' + \Theta' \cot \theta + n(n+1)\Theta &= 0,
\end{aligned} \tag{A.5}$$

which is simply a form of Legendre's Equation. The solutions to Equation A.5 have the form

$$\Theta(\theta) = C \mathcal{P}_n(\cos \theta) + D \mathcal{Q}_n(\cos \theta),$$

with \mathcal{P}_n and \mathcal{Q}_n Legendre functions of the first and second kinds, respectively; however, we can let $D = 0$ because the \mathcal{Q}_n terms have non-physical forms, and so

$$\Theta(\theta) = C \mathcal{P}_n(\cos \theta). \tag{A.6}$$

The R part of Equation A.4 is solved similarly, with

$$\frac{d}{dr} \left(r^2 \frac{d}{dr} R \right) = \left[-\frac{\tau^2}{\alpha^2} r^2 + n(n+1) \right] R$$

$$\begin{aligned}
&\Rightarrow 2rR' + r^2R'' = \left[-\frac{\tau^2}{\alpha^2}r^2 + n(n+1) \right] R \\
&\Rightarrow R'' + \frac{2}{r}R' + \left[\frac{\tau^2}{\alpha^2} - \frac{n(n+1)}{r^2} \right] R = 0.
\end{aligned} \tag{A.7}$$

This is the spherical form of Bessel's Equation, and has solutions

$$R(r) = F j_n\left(r\frac{\alpha}{\tau}\right) + G y_n\left(r\frac{\alpha}{\tau}\right),$$

where j_n and y_n are spherical Bessel functions of the first and second kinds. We discard the y_n terms, because they are non-physical (they go to $-\infty$ at 0), and find

$$R(r) = F j_n\left(r\frac{\alpha}{\tau}\right). \tag{A.8}$$

Combining Equations A.3, A.6, and A.8, our complete solution to Equation A.1 is

$$u(r, \theta, t) = \sum_{n=0}^{\infty} C_n j_n\left(r\frac{\alpha}{\tau}\right) \mathcal{P}_n(\cos \theta) e^{-t\tau^2} \tag{A.9}$$

A.2 Fourier's Trick

Now we must examine the bounds of the problem. The first bound is when $t = 0$, i.e. the steady-state solution. As in many problems, we take the initial condition to be

that everything is at room temperature (T_∞). We thus set

$$u(r, \theta, 0) = \sum_{n=0}^{\infty} C_n j_n\left(r \frac{\alpha}{\tau}\right) \mathcal{P}_n(\cos \theta) = T_\infty, \quad (\text{A.10})$$

and apply Fourier's Trick to this, i.e. use the orthogonality of the functions to find C_n . The orthogonality equation is

$$\begin{aligned} \sum_{n=0}^{\infty} \sum_{p=1}^{\infty} C_{np} \int_0^1 \int_0^\pi j_{n+\frac{1}{2}}\left(r \frac{\alpha}{\tau_{np}}\right) j_{n+\frac{1}{2}}\left(r \frac{\alpha}{\tau_{np'}}\right) P_n(\cos \theta) P_{n'}(\cos \theta) d\theta dr \\ = T_\infty \int_0^1 \int_0^\pi j_{n+\frac{1}{2}}\left(r \frac{\alpha}{\tau_{np'}}\right) P_{n'}(\cos \theta) d\theta dr, \end{aligned}$$

where τ_{np} and $\tau_{np'}$ are such that $\frac{\alpha}{\tau}$ is the p th root of $j_{n+\frac{1}{2}}$ (this arises because Bessel Functions are orthogonal with respect to roots). This simplifies to

$$\begin{aligned} C_{np} = T_\infty \frac{\int_0^1 j_{n+\frac{1}{2}}\left(r \frac{\alpha}{\tau_{np}}\right) dr \int_0^\pi P_n(\cos \theta) d\theta}{\int_0^1 \left[j_{n+\frac{1}{2}}\left(r \frac{\alpha}{\tau_{np}}\right) \right]^2 dr \int_0^\pi [P_n(\cos \theta)]^2 d\theta} \\ = T_\infty \frac{\left(\frac{\tau_{np}}{\alpha} j_{n+\frac{3}{2}}\left(\frac{\alpha}{\tau_{np}}\right) \right) \left(\frac{\sin n\pi}{(n^2+n)\pi} \right)}{\left(j_{n+\frac{3}{2}}\left(\frac{\alpha}{\tau_{np}}\right) \right) \left(\frac{2}{2n+1} \right)}. \quad (\text{A.11}) \end{aligned}$$

We now note that the $\sin n\pi$ term appears to zero all coefficients; however, by convention the singularity at $n = 0$ is often removed from the $\int P_n(\cos \theta) d\theta$ term by setting it equal to 2. Thus we have only $n = 0$ solutions, and simplifying further

yields that

$$C_{np} = T_{\infty} \frac{\left(\frac{\tau_{np}}{\alpha} j_{\frac{3}{2}} \left(\frac{\alpha}{\tau_{\frac{1}{2}p}} \right) \right)}{\left(j_{\frac{3}{2}} \left(\frac{\alpha}{\tau_{\frac{1}{2}p}} \right) \right)}$$

It is here that we run into problems. We know that, in this steady-state solution, the exact value of the function should be simply T_{∞} for all r and θ . The latest solutions we have found for C_{np} have alternating signs in p , and so sum to zero. Therefore there must be a problem in our work, or in our assumptions. The solution to this problem is left as an exercise for the reader.

A.3 Numerical Solutions

Though there are too many parameters to fit for us to make use of numerical methods for approximating u , we can examine the basic nature of u by using dummy values for parameters. An example is seen in Figure A.1, where u is plotted vs. r , and we can see that the function swiftly approaches the constant room temperature as r grows large. We also note that the singularity we remove in our analytical solution is clearly present—and non-physical—in the numeric solution.

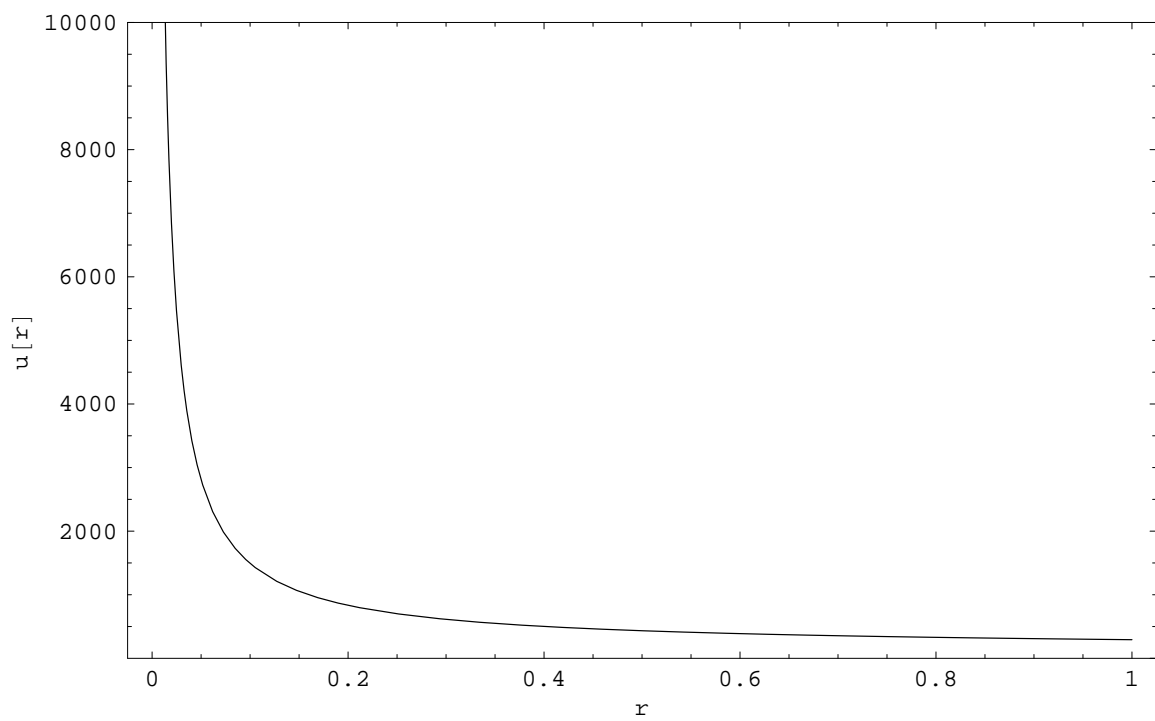


Figure A.1: A numerically-derived solution for u . Note that the function approaches a constant as $r \rightarrow \infty$.

Appendix B

Optical Notes

B.1 Paths, Dispersion, and Gas-Laser Plasma Lines

We use a Helium-Neon laser for excitation. Gas lasers such as this work by electrically stimulating an intermediary gas, which then transfers energy to the emitting gas through collisions. Any emitting gas will have multiple paths through which it can return to ground, and thus multiple spectral lines. While the laser is designed such that only the desired wavelength is stimulated and leaves the laser in a coherent, collimated form, these other ‘plasma’ lines are still present, and can interfere in measurements.

There are numerous ways of removing plasma lines. We made use of three methods in our NFOS setup. First, immediately upon leaving the laser, the beam enters a

prism. This sends the other wavelengths of light leaving the laser off in different directions—most importantly, any plasma light that was randomly emitted collinear with the main beam is cast off. Unfortunately, this can deflect some light that was previously dispersing into the main beam, so we take the beam through a path of approximately 4 meters, giving the superfluous lines room to disperse. Finally, we take the beam through an iris, which blocks all but the core, most-collimated laser light.

In order to prevent the reentry of dispersed and deflected plasma lines into the beam path or NFOS path, during operation we place a number of dark cardboard and paperboard blockers to contain and shield the setup.

B.2 Measuring the NFOS Laser-Focus Width

To measure the width of the focus at the sample, we affixed a thin razor blade aligned with the sample, and placed a photodetector behind to catch the beam. By translating the blade across the focus spot, we get the intensity data in Figure B.1. Also shown in the figure is the derivative of the data, and by examining the FWHM of the derivative peak, we have a good measure of the beam's width—in this case, approximately $10\ \mu\text{m}$.

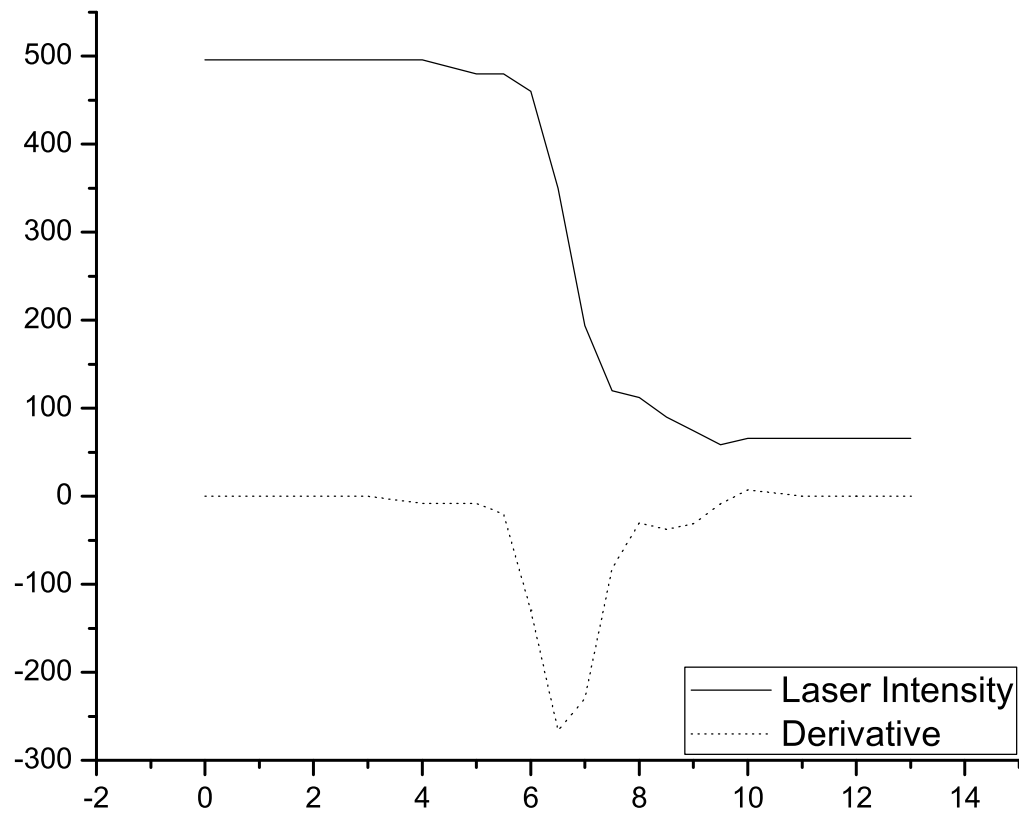


Figure B.1: Laser intensity vs. position for the razor test, as well as the derivative of this data. The FWHM of the derivative peak is a measure of beam width.

Bibliography

- [1] Todd H. Ballinger and Jr. John T. Yates. Ir spectroscopic detection of lewis acid sites on Al_2O_3 using adsorbed CO . correlation with Al-OH group removal. *Langmuir*, 7:3041–3045, 1991.
- [2] T. Chia, L. L. Hench, C. Qin, and C. K. Hsieh. Thermal modeling of laser-densified microlenses. *Applied Optics*, 33, June 1994.
- [3] Taipau Chia, L. L. Hench, Chaobin Quin, and C. K. Hsieh. Laser densification modeling. In Brian J. J. Zelinski, C. Jeffrey Brinker, David E. Clark, and Donald R. Ulrich, editors, *Better Ceramics Through Chemistry IV*, volume 180 of *Better Ceramics Through Chemistry*, pages 819–824, Pittsburgh, 1990. Materials Research Society.
- [4] Inc. Comsol. Model gallery : H-bend microwave waveguide., October 2006.
- [5] Larry L. Hench. *Sol-Gel Silica*. Noyes Data Corporation/Noyes Publications, 1998.

- [6] Brian Henderson and George F. Imbusch. *Optical Spectroscopy of Inorganic Solids*. Clarendon Press, Oxford, 1989.
- [7] Lisa C. Klein, editor. *Sol-Gel Optics: Processing and Applications*. The Kluwer International Series in Engineering and Computer Science. Kluwer Academic Publishers, Boston, 1994.
- [8] M. Lax. Temperature rise induced by a laser beam. *Journal of Applied Physics*, 48(9):3919–3924, September 1977.
- [9] M. Lax. Temperature rise induced by a laser beam ii. the nonlinear case. *Applied Physics Letters*, 33(8):786–788, October 1978.
- [10] B. C. Lippens and J. H. de Boer. Study of phase transformations during calcination of aluminum hydroxides by selected area electron diffraction. *Acta Crystallographica*, 17:1312–1321, 1964.
- [11] Mark Lombardi and Ken Krebs. Unpublished work. (As yet) unpublished work by Lombardi and Krebs on lanthanum impurities and trivalent chromium spectra in alumina.
- [12] D. Rosenthal. The theory of moving heat sources and its application to metal treatments. *Transactions of the American Society of Mechanical Engineers*, 68:849–866, November 1946.

- [13] Todd W. Simpson, Qingzhe Wen, Ning Yu, and David R. Clarke. Kinetics of the amorphous $\rightarrow \gamma \rightarrow \alpha$ transformations in aluminum oxide. *Journal of the American Ceramic Society*, 81:61–66, 1998.
- [14] Satoru Sugano, Yukito Tanabe, and Hiroshi Kamimura. *Multiplets of Transition-Metal Ions in Crystals*. Academic Press, New York, 1970.
- [15] K. Wefers and C. Misra. *Oxides and Hydroxides of Aluminum*. Aluminum Company of America, 1987.
- [16] Bulent E. Yoldas. Alumina gels that form porous transparent Al_2O_3 . *Journal of Materials Science*, 10:1856–1860, 1975.
- [17] Bulent E. Yoldas. Alumina sol preparation from alkoxides. *Ceramic Bulletin*, 54:289–290, 1975.